



# Improved H<sub>2</sub> production of Pt-TiO<sub>2</sub>/g-C<sub>3</sub>N<sub>4</sub>-MnO<sub>x</sub> composites by an efficient handling of photogenerated charge pairs



S. Obregón, G. Colón\*

Instituto de Ciencia de Materiales de Sevilla, Centro Mixto Universidad de Sevilla-CSIC, C/Américo Vespucio, 49, 41092 Sevilla, Spain

## ARTICLE INFO

### Article history:

Received 31 May 2013

Received in revised form 11 July 2013

Accepted 16 July 2013

Available online 11 August 2013

### Keywords:

Pt-TiO<sub>2</sub>

g-C<sub>3</sub>N<sub>4</sub>

MnO<sub>x</sub>

Phenol

H<sub>2</sub> production

## ABSTRACT

Pt-TiO<sub>2</sub>/g-C<sub>3</sub>N<sub>4</sub>-MnO<sub>x</sub> hybrid structures are synthesized by means of a simple impregnation method of Pt-TiO<sub>2</sub> and g-C<sub>3</sub>N<sub>4</sub>-MnO<sub>x</sub>. From the wide structural and surface characterization we have stated that TiO<sub>2</sub>/g-C<sub>3</sub>N<sub>4</sub> composites are formed by an effective covering of g-C<sub>3</sub>N<sub>4</sub> by TiO<sub>2</sub>. The modification of composite by Pt and/or MnO<sub>x</sub> leads to improved photoactivities for phenol degradation reaction. Moreover, enhanced photoactivities have been obtained for composites systems for H<sub>2</sub> evolution reaction. The notably photocatalytic performance obtained was related with the efficient separation of charge pairs in this hybrid heterostructure.

© 2013 Elsevier B.V. All rights reserved.

## 1. Introduction

Taking into consideration the current socioeconomical and environmental situation, it is widely believed that hydrogen will play an important role in this system since it is considered the ultimate clean energy carrier. In this sense, the definitive future effective depletion of fossil fuels as well as the serious environmental problems associated with CO<sub>2</sub> production has inspired the development of viable alternatives. Of these, the solar photocatalytic water splitting reaction in which sunlight and water are used as the hydrogen source is a highly appreciated alternative [1]. Over the last three decades the overall photocatalytic water splitting process has been extensively studied [2–4]. Regarding this field of research, however, it must be said that the earliest research focused more on developing good photocatalysts than on actually understanding the process itself. Thus, in the past decades, numerous methods have been developed to increase the photocatalytic efficiency of TiO<sub>2</sub>, such as cationic doping (Cr, Fe, V) [5], and anionic doping (N, C, B) [6,7] of TiO<sub>2</sub> in order to increase the visible light absorbance. A second approach widely reported passed through the coupling of TiO<sub>2</sub> with other semiconductors [8,9] to increase the separation efficiency of photogenerated electron–hole pairs during photocatalysis mechanism. On this basis, it has been stated that recent

advances in the tailoring of new photocatalysts for solar water splitting might defectively afford the comprehension of the band electronic structure and the effective handling of the photogenerated charge carriers [10].

Within this framework, the improvement and optimization of TiO<sub>2</sub> photocatalyst is an important task for technical applications of heterogeneous photocatalysis in the future [11]. Thus, it is widely accepted that the final photoactivity is strongly affected by the effective migration of generated charge carriers to the surface and its further transfer processes. Therefore many attempts were made for the improvement of the photocatalytic efficiency by inducing the separation of photogenerated charges. Among these approaches some authors invoked the use of noble metal co-catalysts such as Pt, Rh or Au [12,13]. On the other hand, carbon-like materials such as carbon nanotubes, graphene or carbon nitride have also served for this purpose [14–16].

Furthermore Yan et al. described the photocatalytic behavior of g-C<sub>3</sub>N<sub>4</sub>-TiO<sub>2</sub> for the photoinduced hydrogen production reaction [17]. In this case the composite were obtained by ball-milling and further calcination, being the optimal g-C<sub>3</sub>N<sub>4</sub> content at 50 wt%. In a recent paper we reported the preparation of g-C<sub>3</sub>N<sub>4</sub>-TiO<sub>2</sub> composites with different g-C<sub>3</sub>N<sub>4</sub> loading by a simple impregnation method [18]. By platinum and MnO<sub>x</sub> loading the photocatalytic performance of such hybrid systems has been improved and evaluated for H<sub>2</sub> production as well as for phenol degradation under solar-like irradiation.

\* Corresponding author. Tel.: +34 954489536; fax: +34 954460665.  
E-mail address: [gcolon@icmse.csic.es](mailto:gcolon@icmse.csic.es) (G. Colón).

## 2. Materials and methods

### 2.1. Synthesis of photocatalysts

TiO<sub>2</sub> sample was obtained by means of a hydrothermal method elsewhere described [19]. In brief, a TiO<sub>2</sub> colloidal solution was obtained by adding certain amount of Ti<sup>4+</sup>-isopropanol solution to 400 mL of distilled water at pH 2 achieved by means of acetic acid. After TTiP addition a white precipitate is obtained that upon stirring at room temperature for one week evolve to a milky homogeneous solution. A certain amount of triethylamine (TEA) was then added drop wise to the Ti-solution aliquot till the pH value was 9. Afterwards, the obtained white precipitate suspension was then placed in a Teflon recipient inside of stainless steel autoclave reactor. The hydrothermal treatment was performed at 120 °C, 20 h. The as obtained precipitate was then filtered, repeatedly washed and dried overnight at 120 °C. Then TiO<sub>2</sub> powder was submitted to a further calcination treatment at 300 °C for 2 h.

g-C<sub>3</sub>N<sub>4</sub> was obtained by simple calcination of melamine (Aldrich) at 580 °C for 4 h in a covered alumina crucible in order to prevent sublimation of melamine [20].

Carbon nitride-TiO<sub>2</sub> (2 wt% of g-C<sub>3</sub>N<sub>4</sub>) composites were achieved by simple impregnation method [18]. In a typical procedure, the appropriate amounts of g-C<sub>3</sub>N<sub>4</sub> and TiO<sub>2</sub> were added into methanol and sonicated separately for 30 min. Then these two solutions were mixed and stirred at room temperature for 24 h. Afterwards, the composite photocatalysts were obtained by evaporating the methanol under rotary evaporator at 80 °C.

gC<sub>3</sub>N<sub>4</sub>-MnO<sub>x</sub> systems were prepared by wet impregnation method using Mn-acetate as precursor. The final MnO<sub>x</sub> loading was 1 wt%. After impregnation, samples were dried at 120 °C for 20 h and further calcined at 300 °C for 2 h in order to eliminate the organic rest from the precursor.

Platinization was performed over the calcined TiO<sub>2</sub> samples by photodeposition of platinum from hexachloroplatinic (IV) acid (H<sub>2</sub>PtCl<sub>6</sub>, Merck 40% Pt). Suspensions of the different TiO<sub>2</sub> in distilled water were prepared (5 g TiO<sub>2</sub> L<sup>-1</sup>) adding isopropanol to act as sacrificial agent (0.3 M final concentration) and the appropriate amount of H<sub>2</sub>PtCl<sub>6</sub> for a nominal amount of deposited Pt of 1.0% weight total to TiO<sub>2</sub> under continuous nitrogen sparging. Photodepositions were performed by illumination of the suspensions for 3 h with a mercury arc lamp (Ultravitalux, Osram, 300 W). After recovering of the powders by filtration, samples were dried at 110 °C overnight.

### 2.2. Materials characterization

BET surface area and porosity measurements were carried out by N<sub>2</sub> adsorption at 77 K using a Micromeritics 2010 instrument.

X-ray diffraction (XRD) patterns were obtained using a Siemens D-501 diffractometer with Ni filter and graphite monochromator. The X-ray source was Cu K $\alpha$  radiation (0.15406 nm). Crystallite size was calculated from peak broadening using the Scherrer equation by means of XPert HighScore Plus software. The diffraction patterns were recorded from 2 $\theta$  10° to 80° with step of 0.05° and 80 s per step.

The morphology of samples was followed by means of field emission-SEM (Hitachi S 4800) and TEM microscopy (Philips CM 200 microscope). The samples were dispersed in ethanol using an ultrasonicator and dropped on a copper grid.

UV-vis spectra (Shimadzu, AV2101) were recorded in the diffuse reflectance mode (*R*) and transformed to a magnitude proportional to the extinction coefficient (*K*) through the Kubelka-Munk function, *F*(*R* $\infty$ ). Samples were mixed with BaSO<sub>4</sub> that does not absorb in the UV-vis radiation range (white standard). Scans range was 240–800 nm.

XPS data were recorded on 4 × 4 mm<sup>2</sup> pellets, 0.5 mm thick, prepared by slightly pressing the powdered materials which were outgassed in the prechamber of the instrument at room temperature up to a pressure <2 10<sup>-8</sup> to remove chemisorbed water from their surfaces. The Specs spectrometer main chamber, working at a pressure <10<sup>-8</sup> torr, was equipped with a Phoibos 100 multi-channel hemispherical electron analyser with a dual X-ray source working with Mg K $\alpha$  (*h* $\nu$  = 1253.6 eV) at 120 W, 20 mA using C 1s as energy reference (284.6 eV). Surface chemical compositions were estimated from XP-spectra, by calculating the integral of each peak after subtraction of the “S-shaped” Shirley-type background using the appropriate experimental sensitivity factors using UNIFIT 2012 software [21].

### 2.3. Photocatalytic experimental details

Phenol oxidation reactions were performed using a batch reactor (250 mL) using a 300 W UV-vis arc lamp (Ultravitalux, Osram), showing important emission lines at 365 and 420 nm. In the oxidation tests, an air flow was employed what produces a homogenous suspension of the catalyst in the solution. Before each experiment, the catalysts (1 g L<sup>-1</sup>) were settled in suspension with the reagent mixture for 15 min. After this equilibrium time phenol adsorption was in all cases below 3%. The evolution of the initial phenol concentration (ca. 50 ppm) was followed through the evolution of the characteristic 270 nm band using a centrifuged aliquot ca. 2 mL of the suspension (microcentrifuge Minispinn, Eppendorf). The reaction corresponding rates were calculated from C/C<sub>0</sub> vs time curves assuming a zero-order kinetic. The regression coefficients for such fittings are in all cases higher than 0.998.

Photocatalytic H<sub>2</sub> production tests were performed in a flow-reactor system by suspending the powder photocatalysts in an aqueous solution (300 mL, iPrOH/H<sub>2</sub>O 1:11 v/v). The reaction media was continuously thermostated at 30–35 °C to prevent any significant evaporation of the sacrificial agent. The catalyst suspension was firstly degassed with an N<sub>2</sub> stream (150 mL/min) for 30 min. After that the N<sub>2</sub> flow was settled at 15 mL/min and stabilized for 15 min. This nitrogen flow was used to displace the hydrogen produced from the photoreactor headspace toward the GC measuring system. Then, the lamp (Ultravitalux 300 W, Osram) was switched on and the effluent gases were analyzed to quantify H<sub>2</sub> production by gas chromatography (Agilent 490 micro GC) using a thermal conductivity detector connected to a Molsieve 5 A and Pora-LOT Q columns.

## 3. Results and discussion

In Fig. 1 we show the XRD patterns corresponding to the TiO<sub>2</sub>/g-C<sub>3</sub>N<sub>4</sub> composites single and platinized. In all cases the only diffraction pattern present corresponds to the anatase crystalline phase. The obtained TiO<sub>2</sub> systems present in all cases small crystallite size of around 12 nm (Table 1), which is characteristic of the preparation method [19]. In the platinized series (Fig. 1b) additional small diffraction peak at around 2 $\theta$  40° can be associated to the presence of Pt clusters in the surface. The occurrence of an observable Pt diffraction line clearly denotes a notably crystallite size deposits. The diffraction pattern of the pristine g-C<sub>3</sub>N<sub>4</sub> exhibits the typical structure without an impurity phase (Fig. 1c). g-C<sub>3</sub>N<sub>4</sub> typically shows two diffraction peaks at around 13° and 28° which are associated to its layered. The former with a much weaker intensity is related to an in-plane structural packing arrangement parallel to the *c*-axis. Meanwhile the peak at around 28° is attributed to the long-range interplanar stacking of aromatic rings, identified as the (002) peak. For MnO<sub>x</sub> doped g-C<sub>3</sub>N<sub>4</sub> we have not found any trace of MnO<sub>x</sub> diffraction peaks. This could be explained by taking

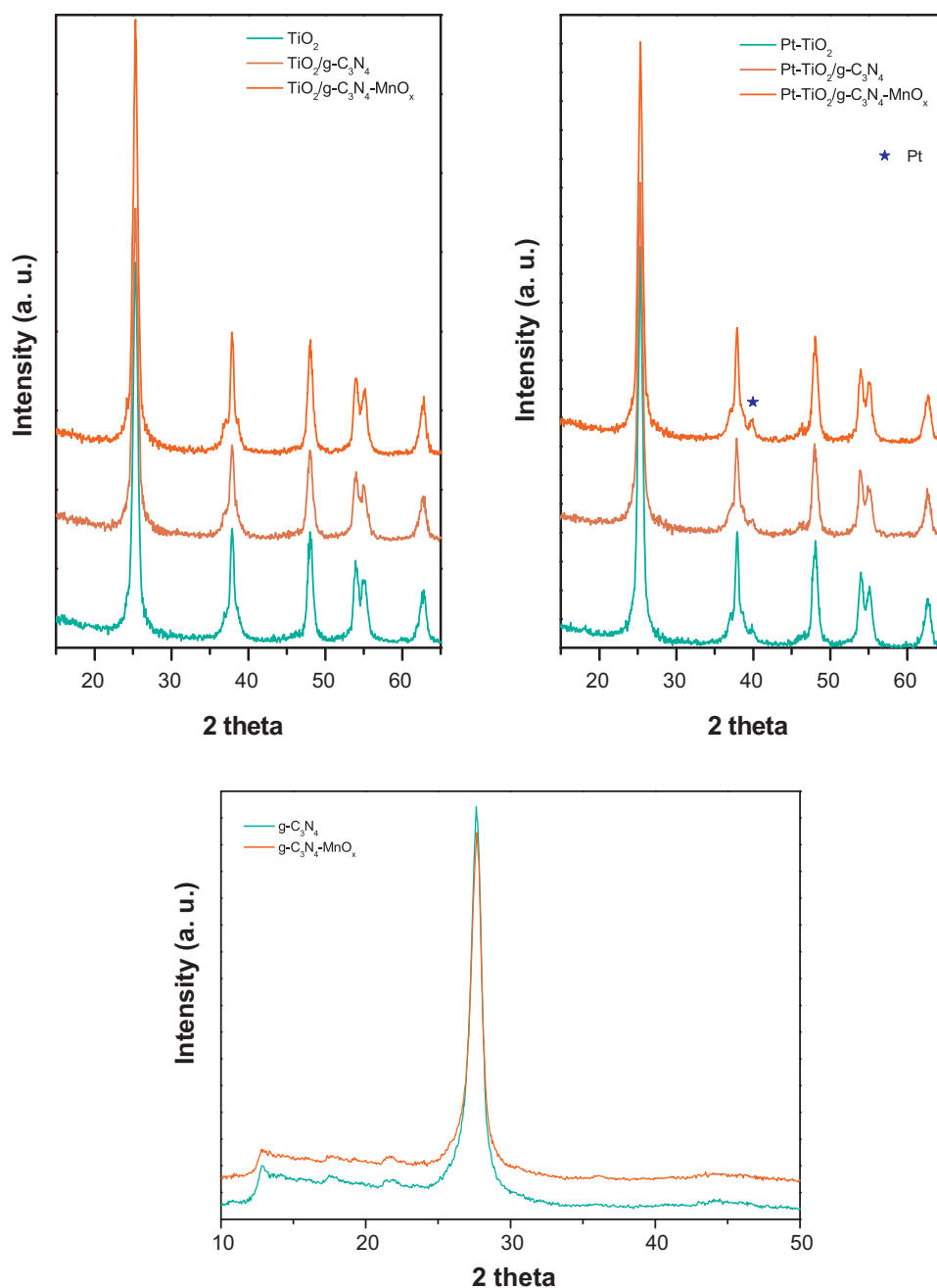


Fig. 1. XRD patterns for a)  $\text{TiO}_2$  and  $\text{TiO}_2/\text{g-C}_3\text{N}_4$  composites and b) platinized catalysts; c) XRD patterns for  $\text{g-C}_3\text{N}_4$  and  $\text{g-C}_3\text{N}_4\text{-MnO}_x$ .

Table 1

Surface and structural characterization for  $\text{TiO}_2\text{-gC}_3\text{N}_4$  composite photocatalysts.

Sample	BET ( $\text{m}^2/\text{g}$ )	Band gap <sup>a</sup> (eV)	Crystallite size (nm)	N/Ti from XPS	Pt/Ti from XPS	Photoactivity		
						Phenol		$\text{H}_2$ evolution (mmol/h/g)
						( $\times 10^{-8}$ mol/L/s)	Eff <sup>b</sup>	
$\text{TiO}_2$	114	3.18	12	0.01	–	3.5	–	–
$\text{TiO}_2/\text{g-C}_3\text{N}_4$	110	3.12	12	0.06	–	4.2	1.20	–
$\text{TiO}_2/\text{g-C}_3\text{N}_4\text{-MnO}_x$	107	3.12	12	0.06	–	4.3	1.23	–
$\text{Pt-TiO}_2$	105	3.20	12	0.01	$3.5 \cdot 10^{-3}$	4.8	–	5.5
$\text{Pt-TiO}_2/\text{g-C}_3\text{N}_4$	107	3.15	13	0.06	$4.0 \cdot 10^{-3}$	7.0	1.46	6.5
$\text{Pt-TiO}_2/\text{g-C}_3\text{N}_4\text{-MnO}_x$	103	3.15	13	0.06	$3.6 \cdot 10^{-3}$	10.6	2.20	7.6

<sup>a</sup> Calculated from  $(\text{KM} \times \text{energy})^n$  plot, considering  $n = 2$  for direct band gap semiconductors

<sup>b</sup> Enhancement factor was calculated from the ratio between each reaction rate with respect to reference  $\text{TiO}_2$  or  $\text{Pt-TiO}_2$ .

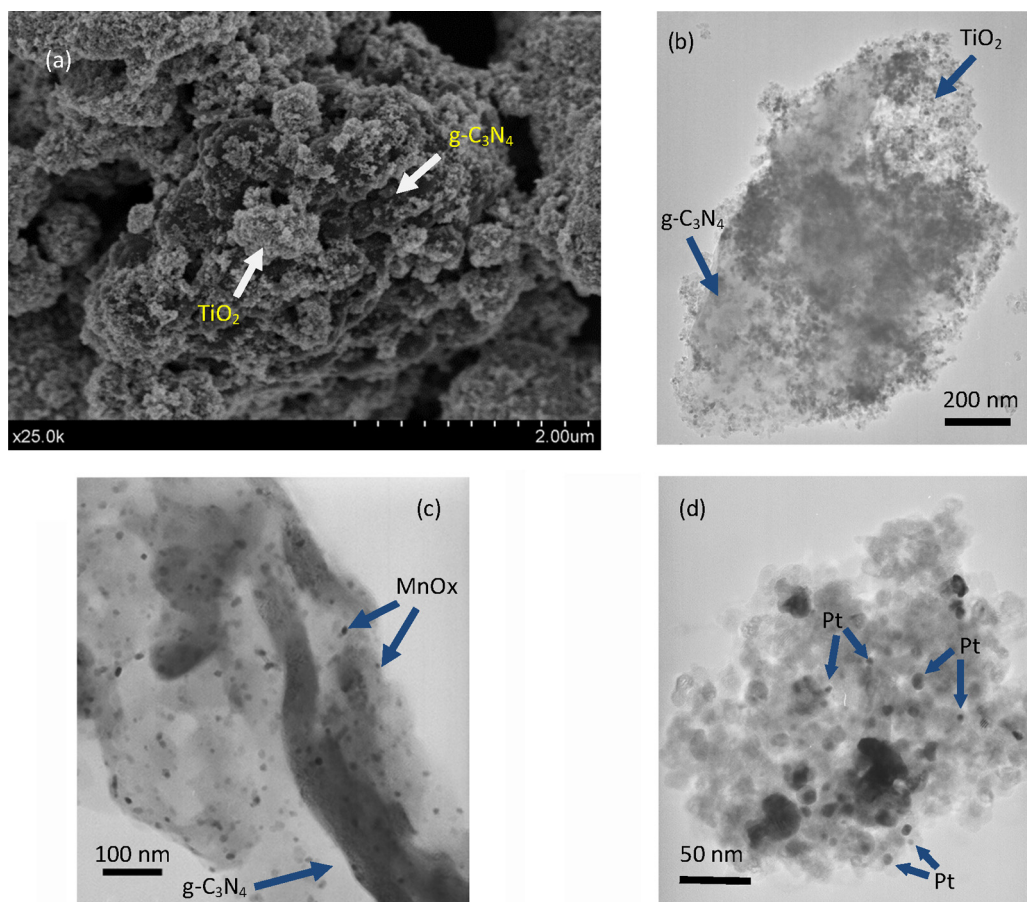


**Fig. 2.** FESEM and TEM images of  $\text{TiO}_2/\text{g-C}_3\text{N}_4\text{-TiO}_2$  composite: a) FESEM and b) TEM image of  $\text{TiO}_2$  deposits on  $\text{g-C}_3\text{N}_4$ ; c) TEM image for  $\text{g-C}_3\text{N}_4\text{-MnO}_x$ ; d) TEM image for  $\text{Pt-TiO}_2/\text{g-C}_3\text{N}_4\text{-MnO}_x$  composite.

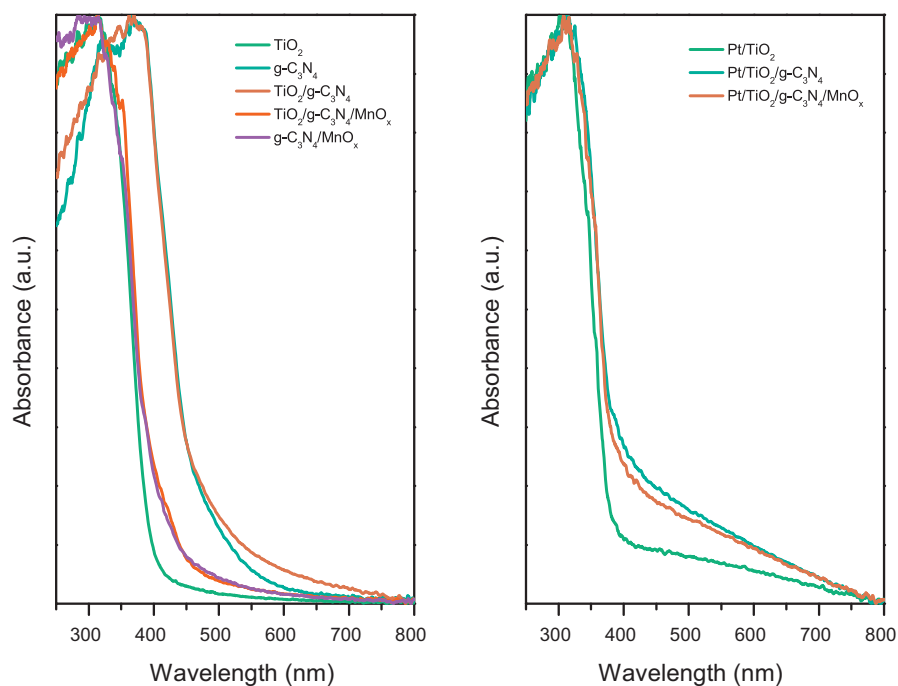


**Fig. 3.** Diffuse reflectance spectra for  $\text{g-C}_3\text{N}_4$ ,  $\text{TiO}_2$  and composites.

into account the low loading level and/or the amorphous feature of  $\text{MnO}_x$ .

In Table 1 we summarize the surface and structural characterization of studied systems. As it can be noticed,  $\text{TiO}_2$  prepared by the hydrothermal sol–gel method exhibits a high surface area value (ca.  $115 \text{ m}^2/\text{g}$ ). Similarly, composite systems show also high BET surface areas around  $110 \text{ m}^2/\text{g}$ . The lower surface area of composite materials is associated to the lower value exhibited by  $\text{g-C}_3\text{N}_4$  which induces such diminution. As it has been previously reported, the impregnation method for preparing the  $\text{TiO}_2/\text{g-C}_3\text{N}_4$  composite notably affects not only the surface area values but also the pore size distribution [18].

From SEM images it can be inferred that the  $\text{TiO}_2$  aggregates effectively cover the large  $\text{g-C}_3\text{N}_4$  particles (Fig. 2a). On the other hand, it can be noticed that  $\text{TiO}_2$  aggregates are formed by small sphere-like structure with an average diameter of 15–20 nm with a very homogeneous size distribution (Fig. 2b). This fact is in accordance with the crystallite size calculated from XRD. From TEM image it has been also stated that the incorporation of  $\text{MnO}_x$  in the  $\text{g-C}_3\text{N}_4$  support by wet impregnation leads to a homogenous distribution of  $\text{MnO}_x$  aggregates of around 10–15 nm size (Fig. 2c). Regarding to Pt deposits, it can be noticed that photodeposition method leads to the formation of Pt clusters with heterogeneous size distribution (Fig. 2d). Thus, Pt aggregates exhibit size range between 4 nm and 10 nm.

As it has been previously reported,  $\text{TiO}_2/\text{g-C}_3\text{N}_4$  composites present a small absorption shoulder in addition to the typical absorption band of  $\text{TiO}_2$  (Fig. 3). This absorption at lower energy corresponds to the presence of  $\text{g-C}_3\text{N}_4$ . Indeed, the main absorption edge of pristine  $\text{g-C}_3\text{N}_4$  takes place at around 435 nm, being the band gap energy ca. 2.85 eV. The calculated band gap values for all composite systems are similar to that showed by  $\text{TiO}_2$ , and are located around 3.12–3.20 eV. For platinized series it can be noticed a small broad absorption band along the visible range which can be attributed to the surface plasmon resonance (SPR) of the loaded Pt nanoparticles [22].

The surface chemical composition of composites was studied by XPS (Fig. 4). The presence of platinum deposits was stated by the small Pt 4f signal (Fig. 4a). As it can be seen, platinized series show a small and not-defined wide band at around 69–78 eV. Within this range it can be ascribed the corresponding Pt 4f level for  $\text{Pt}^0$  as well as for Pt oxidized states [13]. Although, low signals do not allow us to calculate the amount of oxidized species, since the 4f doublet appears not well-defined and broad, the presence of  $\text{Pt}^{2+}$  and  $\text{Pt}^{4+}$  species are expected. The quantification of this signal, similar amounts of Pt arise for all platinized samples (Table 1). This would indicate that photodeposition process has proceeded similarly for all systems.

Regarding to the N 1s spectrum several binding energies can be deconvoluted for pristine  $\text{g-C}_3\text{N}_4$  (inset in Fig. 4b). The three peaks found could be ascribed to C–N–C at 397.7 eV, N–(C)<sub>3</sub> at 398.7 eV and N–H at 400.6 eV [23,24]. The average C/N ratio calculated in our case is 0.71, in accordance with values reported for  $\text{g-C}_3\text{N}_4$  obtained this way [25]. For composite  $\text{TiO}_2/\text{g-C}_3\text{N}_4$  systems the N 1s signal appears equally (Fig. 4) and gives a N/Ti ratio of 0.06 in all cases (Table 1). It can be noticed that for bare  $\text{TiO}_2$  a small N 1s band located at 399.4 eV is also present. This small contribution would indicate a small residue from triethylamine used in the preparation procedure.

We have also performed the XPS analysis for  $\text{g-C}_3\text{N}_4\text{-MnO}_x$  system (Fig. 5). Manganese oxides are generally expressed with the chemical formula of  $\text{MnO}_x$ , due to the multiple valence states exhibited by Mn [26]. The Mn 2p region consists of a spin–orbit doublet with binding energy centered at ca. 654 eV (Mn 2p<sub>1/2</sub>), which are characteristics of a mixed-valence manganese system ( $\text{Mn}^{4+}$ ,  $\text{Mn}^{3+}$  and  $\text{Mn}^{2+}$ ).

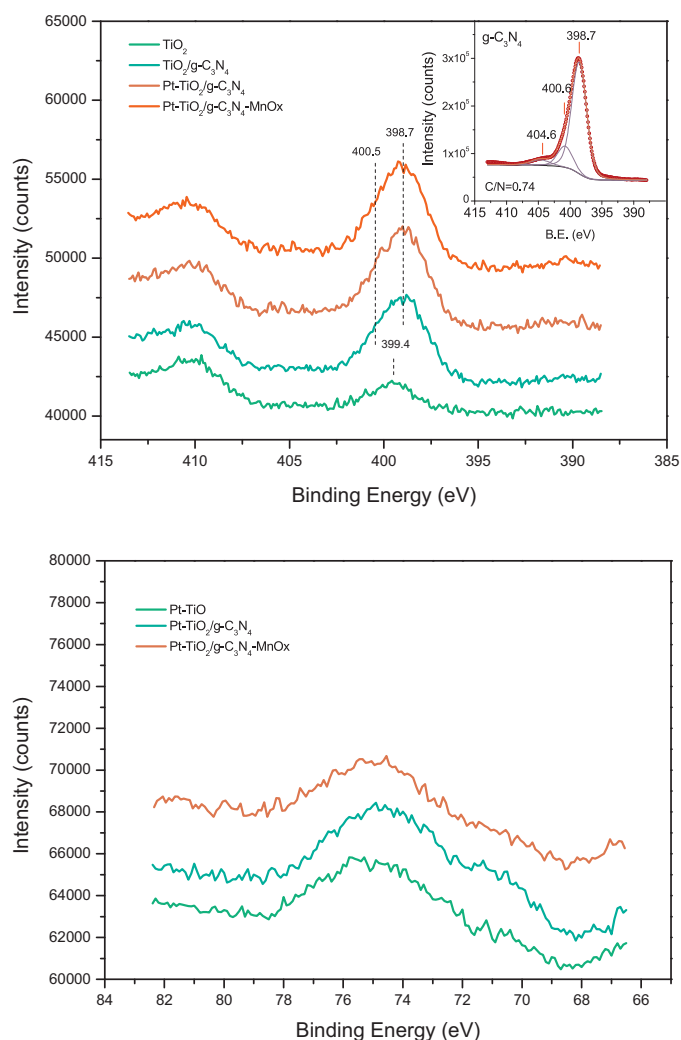


Fig. 4. X-ray photoelectron spectra of a) N 1s level for different  $\text{TiO}_2/\text{g-C}_3\text{N}_4$  composites. Inset plot show the deconvolution analysis of the corresponding spectra for  $\text{g-C}_3\text{N}_4$ ; b) Pt 4f level for platinized composites.

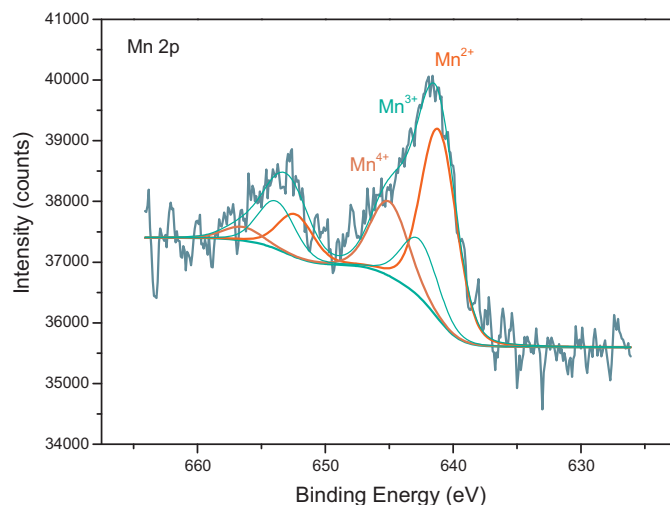
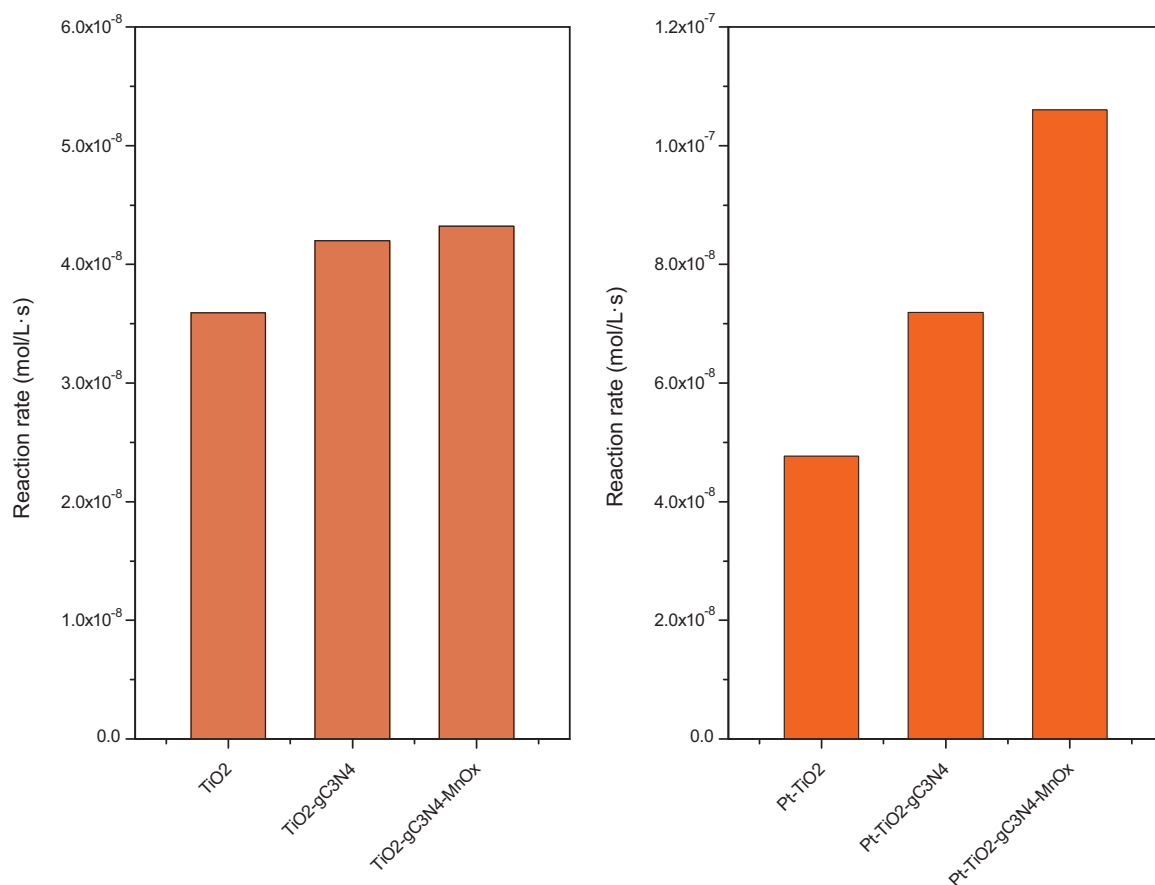
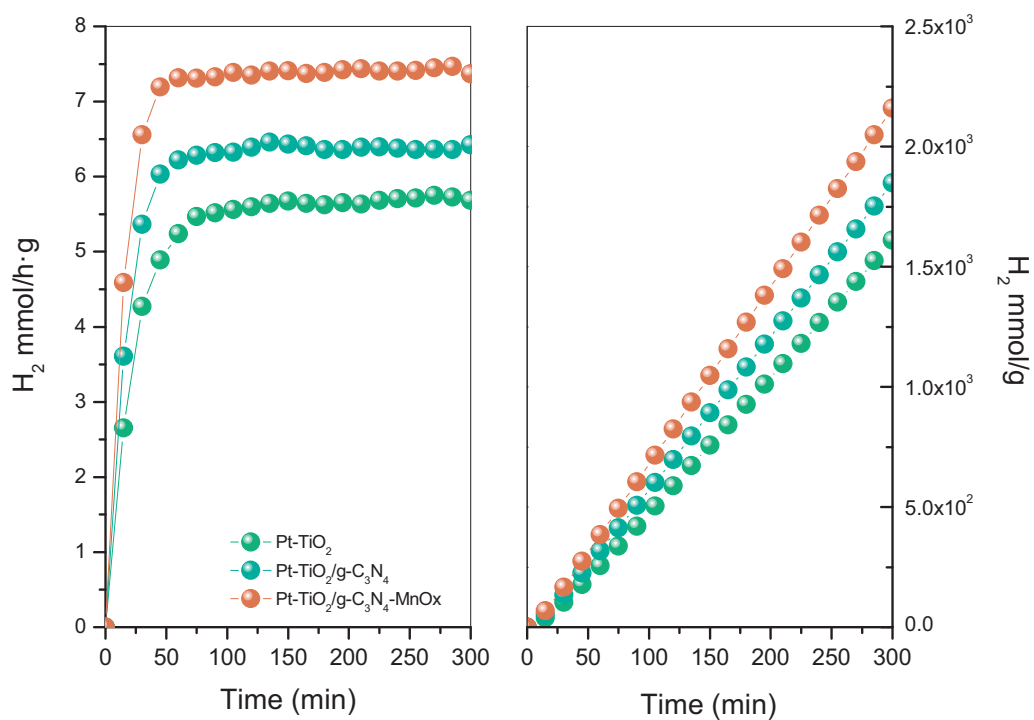


Fig. 5. X-ray photoelectron spectra of Mn 2p level for  $\text{g-C}_3\text{N}_4\text{-MnO}_x$ .

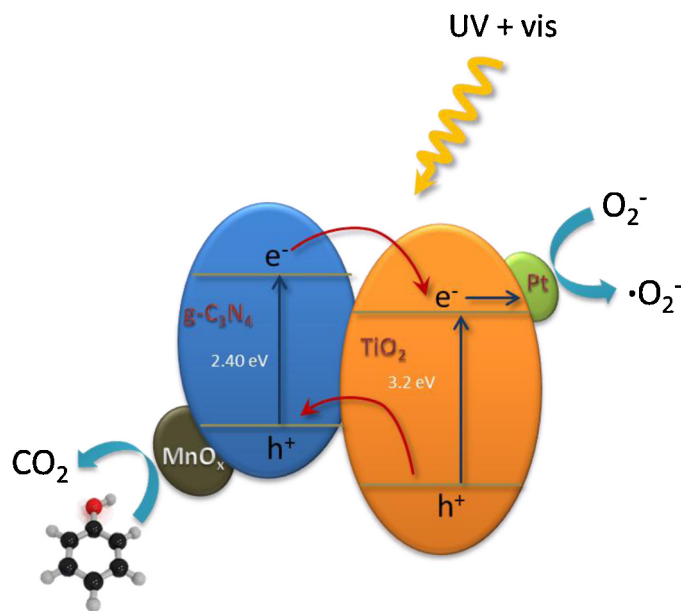




**Fig. 6.** Evolution of phenol with photodegradation time for TiO<sub>2</sub> and TiO<sub>2</sub>/g-C<sub>3</sub>N<sub>4</sub> composite photocatalysts.



**Fig. 7.** Evolution of H<sub>2</sub> production for different platinumized TiO<sub>2</sub> and TiO<sub>2</sub>/g-C<sub>3</sub>N<sub>4</sub> composite photocatalysts: a) Reaction rate and b) Hydrogen evolution with time.



Scheme 1.

In order to evaluate the photocatalytic performance of the  $\text{TiO}_2/\text{g-C}_3\text{N}_4$  composites we have studied the photocatalytic degradation of phenol and the  $\text{H}_2$  production reactions. This way, we would estimate both oxidation and reduction behavior of the photocatalysts. For phenol photooxidation reaction, it is clear that the formation of a  $\text{TiO}_2/\text{g-C}_3\text{N}_4$  composite leads to higher photocatalytic activities (Fig. 6). The incorporation of  $\text{MnO}_x$  as co-catalyst does not seem to enhance significantly the photoactivity of our system. Thus, the enhancement factor ( $E_f$ , defined as the ratio of each reaction rate with respect to single  $\text{TiO}_2$  or  $\text{Pt-TiO}_2$ ) for composite appears similar (Table 1). However, for platinized series the conjunction of both co-catalysts leads to a remarkably improvement in the photoactivity. The calculated enhancement factor for composites clearly denotes that the occurrence of Pt and  $\text{g-C}_3\text{N}_4$  and more pronounced the occurrence of Pt and  $\text{g-C}_3\text{N}_4\text{-MnO}_x$  lead to improved photocatalytic situation (Table 1).

The photocatalytic  $\text{H}_2$  production rates over different platinized  $\text{TiO}_2/\text{g-C}_3\text{N}_4$  composites are shown in Fig. 7. The photoreduction rates plainly show that composite system has higher photocatalytic activity. In all cases, this reaction rate shows a quite stable value along the reaction time, indicating the stability of the catalyst. The observed enhancement is more evident for Pt and  $\text{MnO}_x$  co-doped system. The  $E_f$  values clearly denote a synergistic effect which takes place in this composite (Table 1).

The scheme for electron–hole separation and transport at the light driven  $\text{TiO}_2/\text{g-C}_3\text{N}_4$  hybrid photocatalyst can be discussed as follows: the conduction and valence band edge potentials for  $\text{g-C}_3\text{N}_4$  were located at  $-1.12$  and  $1.57$  eV, respectively [27]. Thus, the photoexcited electrons on  $\text{g-C}_3\text{N}_4$  can transfer easily to the  $\text{TiO}_2$  conduction band while holes would be promoted toward the  $\text{g-C}_3\text{N}_4$  valence band. In other words,  $\text{TiO}_2$  can act as a sink for photoexcited electrons while  $\text{g-C}_3\text{N}_4$  for holes, hindering this way the charge recombination process. Within this scheme, we have previously reported that a synergetic electronic mechanism between both systems would take place [18]. For  $\text{TiO}_2/\text{g-C}_3\text{N}_4\text{-MnO}_x$  we have observed similar reaction rates for phenol degradation. This result would be in accordance with the above electronic flow diagram, since  $\text{MnO}_x$  would slightly exalt holes migration and transfer (Scheme 1). Therefore, the probability of electron–hole recombination was reduced as well as enhanced the separation efficiency. For platinized systems, we have assembled an extra

electron sink site. Pt nanoparticles deposited on  $\text{TiO}_2$  surface would favor the electron transfer toward  $\text{TiO}_2$  and charge separation in  $\text{g-C}_3\text{N}_4$  would be more efficient due to the formed Schottky barrier at the interfaces of the Pt and  $\text{TiO}_2$  nanoparticles (Scheme 1). This fact would point out that the differences in the conduction band edge potentials between  $\text{TiO}_2$  and  $\text{g-C}_3\text{N}_4$  are probably a more powerful driving force, which favors electron flow from  $\text{g-C}_3\text{N}_4$  to  $\text{TiO}_2$  nanoparticles. Therefore, a significant cooperative mechanism would be envisaged from the simultaneous loading with Pt and  $\text{MnO}_x$  co-catalysts. The improved photoinduced charge separation leads to better photocatalytic performance for photooxidation and especially for photoreduction reactions.

#### 4. Conclusions

We have obtained a highly active  $\text{Pt-TiO}_2/\text{g-C}_3\text{N}_4\text{-MnO}_x$  composite by a simple impregnation method. The incorporation of Pt and  $\text{MnO}_x$  co-catalysts in the  $\text{TiO}_2/\text{g-C}_3\text{N}_4$  composite clearly denotes a significant improvement in the photocatalytic activity. Such markedly increase in the photoactivity might be related with the participation of Pt and  $\text{g-C}_3\text{N}_4\text{-MnO}_x$  in the charge separation process. The remarkable enhancement for  $\text{H}_2$  production over the present  $\text{Pt-TiO}_2/\text{g-C}_3\text{N}_4\text{-MnO}_x$  nanocomposite can be attributed not only to photoexcited electrons at  $\text{TiO}_2$ , but also to those of  $\text{g-C}_3\text{N}_4$  directionally migrating to  $\text{Pt-TiO}_2$  due to the close interfacial connections between  $\text{Pt-TiO}_2$  and  $\text{g-C}_3\text{N}_4$ . Similarly the photogenerated holes would proceed efficiently toward  $\text{g-C}_3\text{N}_4\text{-MnO}_x$ , enhancing the photooxidation reaction. This way, electrons and photogenerated holes are efficiently separated in space, which is beneficial for retarding the charge recombination and improving the photoactivity for  $\text{H}_2$  production. As a result, the higher efficiency achieved in the electronic step is responsible for the enhanced photocatalytic activity for phenol photodegradation and hydrogen production reactions. We have stated that by the adequate tailoring of the catalysts it is possible to optimize the charge carriers handling and hinder the recombination process.

#### Acknowledgements

Financial support from P09-FQM-4570 and ENE2011-24412 projects is fully acknowledged. S. Obregón thanks CSIC for the concession of a JAE-Pre grant.

#### References

- [1] A. Kubacka, M. Fernández-García, G. Colón, *Chemical Reviews* 112 (2012) 1555–1614.
- [2] A. Kudo, Y. Miseki, *Chemical Society Reviews* 38 (2009) 253–278.
- [3] R. Abe, *Journal of Photochemistry and Photobiology C: Photochemistry Reviews* 11 (2010) 179–209.
- [4] K. Maeda, *Journal of Photochemistry and Photobiology C: Photochemistry Reviews* 12 (2011) 237–268.
- [5] F. Lin, D.M. Jiang, X.M. Ma, *Journal of Alloys Compounds* 470 (2009) 375–378.
- [6] S.Z. Chen, P.Y. Zhang, D.M. Zhuang, W.P. Zhu, *Catalysis Communications* 5 (2004) 677–680.
- [7] J.J. Xu, Y.H. Ao, D.G. Fu, C.W. Yuan, *Colloids and Surfaces A* 334 (2009) 107–111.
- [8] F. Dong, W.R. Zhao, Z.B. Wu, *Nanotechnology* 19 (2008) 365607.
- [9] S.K. Poznyak, D. Talapin, A. Kulak, *Journal of Physical Chemistry B* 105 (2001) 4816–4823.
- [10] M. Woodhouse, B.A. Parkinson, *Combinatorial approaches for the identification and optimization of oxide semiconductors for efficient solar photoelectrolysis*, *Chemical Society Reviews* 38 (2009) 197–210.
- [11] G. Colón, C. Belver, M. Fernández-García, in: J.A. Rodríguez, M. Fernández-García (Eds.), *Synthesis, Properties and Applications of Solid Oxides*, Wiley, New York, 2007, pp. 491–562.
- [12] M.C. Hidalgo, M. Maicu, J.A. Navío, G. Colón, *Journal of Physical Chemistry C* 113 (2009) 12840–12847.
- [13] G. Colón, M. Maicu, M.C. Hidalgo, J.A. Navío, A. Kubacka, M. Fernández-García, *Journal of Molecular Catalysis A: Chemical* 320 (2010) 14–18.
- [14] N. Zhang, Y. Zhang, Y.J. Xu, *Nanoscale* 4 (2012) 5792–5813.

- [15] P. Niu, L. Zhang, L. Liu, H.M. Cheng, *Advanced Functional Materials* 22 (2012) 4763–4770.
- [16] S. Zhao, S. Chen, H. Yu, X. Quan, *Separation and Purification Technology* 99 (2012) 50–54.
- [17] H. Yan, H. Yang, *Journal of Alloys and Compounds* 509 (2011) L26.
- [18] C. Miranda, H. Mansilla, S. Obregón, G. Colón, *Journal of Photochemistry and Photobiology A: General* 253 (2013) 16–21.
- [19] M.C. Hidalgo, M. Aguilar, M. Maicu, J.A. Navío, G. Colón, *Catalysis Today* 129 (2007) 50–58.
- [20] S.C. Yan, Z.S. Li, Z.G. Zou, *Langmuir* 25 (2009) 10397–10401.
- [21] R. Hesse, Unifit for Windows: Spectrum Processing, Analysis and Presentation Software for Photoelectron Spectra, Version 2012, Leipzig, <<http://www.unifit-software.de/>>.
- [22] J.G. Yu, L.F. Qi, M. Jaroniec, *Journal of Physical Chemistry C* 114 (2010) 13118–13125.
- [23] S.H. Bian, Z. Ma, W.G. Song, *Journal of Physical Chemistry C* 113 (2009) 8668–8672.
- [24] F. Dong, L.W. Wu, Y.J. Sun, M. Fu, Z.B. Wu, S.C. Lee, *Journal of Materials Chemistry* 21 (2011) 15171–15174.
- [25] A. Thomas, A. Fischer, F. Goettmann, M. Antonietti, J.O. Muller, R. Schlogl, J.M. Carlsson, *Journal of Materials Chemistry* 18 (2008) 4893–4908.
- [26] Z. Chen, Q. Yang, H. Li, X. Li, L. Wang, S.C. Tsang, *Journal of Catalysis* 276 (2010) 56–65.
- [27] X.C. Wang, K. Maeda, A. Thomas, K. Takanabe, G. Xin, J.M. Carlsson, K. Domen, M. Antonietti, *Nature Materials* 8 (2009) 76–80.